

HiSST: 4th International Conference on High-Speed Vehicle Science Technology 22 -26 September 2025, Tours, France



Effects of Boundary Layer Transition on Dynamic Stability for Hypersonic Blunt-Cone Vehicles

Li Jiahao¹, Wang Liang², Zhao Ru², Sha Xinguo⁴, Wang Yutang⁵

Abstract

During near-space hypersonic flight, boundary-layer transition strongly affects the aerodynamic stability of reentry vehicles. In this study, the Fu–Wang transition model is applied to investigate the dynamic stability of a hypersonic blunt-cone vehicle under forced pitching oscillations. Numerical simulations are conducted to track the evolution of the transition location and its influence on aerodynamic loads and dynamic responses. Results show that vehicle stability deteriorates as the transition point moves upstream, with the most severe instability occurring when the transition coincides with the center of gravity. Parametric studies further reveal that oscillation amplitude and frequency exert non-monotonic effects on dynamic derivatives, governed by the interplay between viscous unsteadiness and added-mass contributions. These findings highlight the critical role of transition in dynamic stability prediction and provide guidance for transition-control strategies in hypersonic vehicle design.

Keywords: hypersonic, transition, dynamic stability, Fu–Wang transition model

Nomenclature

HiSST-2025-#271 Page | 1 Effects of Boundary Layer Transition on Dynamic Stability for Hypersonic Blunt-Cone Vehicles Copyright © 2025 by author(s)

¹ School of Aerospace Engineering, Tsinghua University, Beijing 100084, China

² School of Aerospace Engineering, Tsinghua University, Beijing 100084, China, <u>wangliang12@tsinghua.edu.cn</u>

³ Beijing Institute of Technology, Beijing 100081, China

⁴ China Academy of Aerospace Aerodynamics, Beijing 100081, China

⁵ China Academy of Launch Vehicle Technology, Beijing 100081, China

C_m – Pitching moment coefficient about C.G.

C_{ma} – Pitching moment slope coefficien

C_{mq} – Pitching moment derivative due to rate of pitching

C_{må} – pitching moment derivative due to rate of change of angle of attack

 E_u – Mean kinetic energy of the flow(relative to the wall). E_u =0.5×(U-U_w)²

ζ_{eff} − Effective length scale

Ma – Mach number

 Ω – Vorticity

P_k – Turbulent kinetic energy production term

 P_{ω} – Specific dissipation rate production term

Re – Reynolds number per unit length

S_{ii} – Mean strain rate tensor

Tu – Free stream turbulence

U_e – Boundary layer edge velocity

U(y_s) – Flow velocity at the generalized inflection point

a - Speed of sound

 α_0 – Initial angle of attack

 $\rho-\text{Dendity}$

t - Time

c_r – Perturbation phase velocity

d - Distance to the wall

γ – Intermittency

k – Turbulent kinetic energy

k_{red} – Reduce frequency

 μ_{eff} – Effective viscosity

μ_{nt} – Non-turbulent viscosity

 μ_t – viscosity

T_{nt} – Time scale of unstable disturbance waves

 τ_{cross} – Time scale associated with crossflow mode

1. Introduction

When operating in near-space hypersonic regimes, reentry vehicles experience complex flow phenomena including shock wave/boundary layer interactions and vortex breakdown, which generate significant unsteady and nonlinear aerodynamic effects[1,2]. These phenomena frequently produce dynamic loads exceeding design specifications and may precipitate catastrophic flight instability incidents. The conceptual framework for characterizing vehicle dynamic stability was first established by Bryan[3,4] in 1911 through the introduction of dynamic derivatives and stability coefficients - an aerodynamic modeling methodology that has endured for over a century in flight mechanics research.

However, accurate prediction of hypersonic vehicle dynamic stability presents substantial challenges due to strongly coupled multiphysics interactions[5]. The complex interplay between aerodynamic forces, thermal environment, structural response, and control system dynamics renders this problem particularly intricate.

Conventional experimental approaches, including both forced-oscillation and free-oscillation wind tunnel testing, face inherent limitations in achievable Mach numbers and measurement precision[6]. Computational studies similarly encounter difficulties[7], as the numerical complexity of free-oscillation simulations necessitates reliance on forced-oscillation methodologies. While RANS-based turbulence modeling remains widely employed for stability analysis, boundary layer transition becomes unavoidable in the high-Reynolds-number flow conditions characteristic of blunt-cone reentry vehicles[8]. Flight test data from early blunt-cone vehicles notably demonstrate that transition processes frequently coincide with pronounced pitch instability events, underscoring the critical relationship between boundary layer transition and dynamic stability characteristics[9].

For transition prediction, the Fu-Wang model[10,11] has demonstrated particular efficacy in simulating hypersonic boundary layer transition. This investigation employs this advanced model to systematically examine the influence mechanisms of boundary layer transition on dynamic stability for blunt-cone reentry vehicles under near-space hypersonic conditions. The research objectives focus on providing theoretical foundations for enhanced stability design and control methodologies in hypersonic flight systems.

2. Numerical method

The present computations were performed using the in-house hypersonic flow simulation code TRANS, developed by the research group. The governing equations are solved in a finite-volume framework. Time integration is carried out with an implicit LU-SGS scheme[12]. The inviscid fluxes are evaluated using the AUSM+_up scheme[13], providing accurate shock-capturing capability while maintaining robustness in high-speed regimes.

2.1. Baseline Transition Model

The Fu–Wang transition model is a three-equation framework. It is derived from linear stability analysis and implemented within the SST turbulence model[14] by introducing a transport equation for the intermittency factor γ . In addition, the eddy viscosity terms in the production source terms of the turbulent kinetic energy and specific dissipation rate transport equations are modified to use the effective viscosity. The governing equations of the model can be expressed as follows:

$$\frac{\partial(\rho k)}{\partial t} + \frac{\partial(\rho u_j k)}{\partial x_j} = \frac{\partial}{\partial x_j} \left[\left(\mu + \sigma_k \mu_{eff} \right) \frac{\partial k}{\partial x_j} \right] + P_k - \beta^* \rho \omega k \tag{1}$$

$$\frac{\partial(\rho\omega)}{\partial t} + \frac{\partial(\rho u_j \omega)}{\partial x_j} = \frac{\partial}{\partial x_j} \left[\left(\mu + \sigma_\omega \mu_{eff} \right) \frac{\partial \omega}{\partial x_j} \right] + P_\omega - \beta_2 \rho \omega^2 - 2(1 - F_1) \frac{\rho \sigma_{\omega 2}}{\omega} \frac{\partial k}{\partial x_j} \frac{\partial \omega}{\partial x_j}$$
 (2)

$$\frac{\partial(\rho\gamma)}{\partial t} + \frac{\partial(\rho u_j \gamma)}{\partial x_j} = \frac{\partial}{\partial x_j} \left[\left(\mu + \frac{\mu_{eff}}{\sigma_{\gamma}} \right) \frac{\partial \gamma}{\partial x_j} \right] + (1 - \gamma) P_{\gamma}$$
(3)

where

$$P_{k} = 2\mu_{eff} \left(S_{ij} S_{ij} - \frac{1}{3} S_{kk} S_{ll} \right) + \frac{2}{3} S_{kk} \rho k \tag{4}$$

$$P_{\omega} = \alpha \frac{\rho}{\mu_t} P_k \tag{5}$$

The physical significance of the effective viscosity, μ_{eff} , lies in the fact that, when the flow becomes fully turbulent, its value reduces to the conventional turbulent viscosity, μ_t . In the transitional regime, however, the effective viscosity is required to reflect the influence of unstable disturbance waves within the laminar boundary layer. Accordingly, its expression is given as:

$$\mu_{eff} = (1 - \gamma)\mu_{nt} + \gamma\mu_t \tag{6}$$

The modeling of the non-turbulent eddy viscosity coefficient, μ_{nt} , is formulated in a manner similar to that of the turbulent eddy viscosity, μ_{t} , in conventional turbulence models:

$$\mu_{nt} = C_{\mu} \rho k \tau_{nt} \tag{7}$$

 τ_{nt} denotes the time scale of unstable disturbance waves. It is composed of three parts: the first-mode time scale τ_{nt1} , the second-mode time scale τ_{nt2} , and the crossflow-mode time scale τ_{cross} , which correspond to the Tollmien–Schlichting (TS) waves in incompressible flows, the Mack waves in compressible flows, and the crossflow instability waves in three-dimensional boundary layers, respectively. The expression is given as:

$$\tau_{nt1} = C_4 \left[\zeta_{eff}^{1.5} / \sqrt{(2E_u)^{0.5} \nu} \right] \tag{8}$$

$$\tau_{nt2} = C_5[2\zeta_{eff}/U(y_s)] \tag{9}$$

The local relative Mach number is defined as:

$$M_{rel} = (U - c_r)/a \tag{10}$$

In the region of a two-dimensional boundary layer where the local relative Mach number exceeds unity, the second mode is the most unstable among the higher-order modes. Therefore, the transition model neglects all higher-order modes except the second mode, and the corresponding time scale is modeled as:

$$\tau_{nt} = \begin{cases} \tau_{nt1}, & |M_{rel}| \le 1\\ \tau_{nt1} + \tau_{nt2}, & |M_{rel}| > 1 \end{cases}$$
 (11)

For a three-dimensional boundary layer, crossflow instability waves often exist in the spanwise direction. In the transition model, the time scale associated with the crossflow mode is formulated as:

$$\tau_{cross} = C_{10}(4\zeta_{eff}/U_e) \times \{-exp[-C_{11}(\zeta_{eff}U_e/v_{eff} - 44)^2]\} \times (W/U_e)^{C_{12}}$$
 (12)

Where: $C_{10}=90$, $C_{11}=0.001$, $C_{12}=0.5$.

The overall time scale is defined as:

$$\tau_{nt} = \tau_{nt1} + \tau_{nt2} + \tau_{cross} \tag{13}$$

 ζ_{eff} denotes the effective length scale, whose modeled form is given as:

HiSST-2025-#271 Page |3

$$\zeta_{eff} = \min \{ C_1 \frac{d^2 \Omega}{\sqrt{2E_\mu}}, C_2 \frac{\sqrt{k}}{(\beta^* \omega)}, C_3 \frac{\sqrt{k}}{(C_\mu | S|)} \}$$
 (14)

Which represent the first, second, and third characteristic length scales, respectively. The production term of the intermittency factor is expressed as:

$$P_{\gamma} = C_9 \rho f(Tu) F_{onset} \left[-\ln(1 - \gamma) \right]^{0.5} \left(1 + C_6 \frac{k^{0.5}}{(2E_u)^{0.5}} \right) \frac{d}{\nu} \left| \nabla E_u \right|$$
 (15)

where the function Fonset determines the onset location of transition:

$$F_{onset} = 1 - \exp\left(-C_7 \frac{\zeta_{eff} k^{0.5} |\nabla k|}{\nu |\nabla E_u|}\right)$$
 (16)

and the term f(Tu) represents the free-stream turbulence intensity function[15]. For bypass transition problems with high free-stream turbulence intensity, its expression is given as:

$$f(Tu) = \sqrt{1.25 \times 10^{-11} \text{Tu}^{7/4}} \tag{17}$$

The construction of the production term for the intermittency factor ensures that its value remains minimal outside the boundary layer, while approaching unity in the near-wall turbulent region. As a result, the wall distribution of the intermittency factor provides a clear indication of the laminar and turbulent regions. The model constants used in the present study are:

Table 1. Model parameters

C1	C2	С3	C4	C5	C6	C7	C8	С9
0.32	7000	0.6	2.2	5.0	0.09	1.15	0.07	486.6

2.2. Dynamic derivative

The concept of dynamic derivatives in flight stability analysis was first introduced by Bryan. In his framework, the problems of aerodynamics and flight dynamics were treated in a decoupled manner, and aerodynamic forces and moments were expressed as functions of state variables. Building upon this idea, Etkin[16,17] formulated the modern definition of dynamic derivatives by expanding aerodynamic forces and moments in a Taylor series with respect to the dynamic parameters. This formulation, which enables the linearization of unsteady aerodynamic responses, has since become a cornerstone of flight stability analysis. In contemporary research, dynamic derivatives are routinely determined through wind tunnel tests (using forced-oscillation or free-oscillation methods) and computational simulations, serving as a fundamental basis for predicting and assessing the dynamic stability of flight vehicles.

For pitching motion, the dynamic derivatives are usually expressed as the derivatives of the pitching moment with respect to the angle of attack and its time rate of change. The pitching moment coefficient can be written as:

$$C_{\rm m} = C_{\rm m_0} + C_{\rm m_\alpha} \alpha + C_{\rm m_\alpha} \frac{\alpha c}{2 I_{\rm loc}} + C_{\rm m_q} \frac{q c}{2 I_{\rm loc}} + \cdots$$
 (18)

where $C_{m_{\alpha}}$ denotes the static stability derivative, while $C_{m_{\dot{\alpha}}}$ and $C_{m_{q}}$ represent the dynamic derivatives associated with the rate of change of angle of attack and the pitch rate, respectively. q denotes the pitch rate of the vehicle. In dynamic derivative analysis, the value of $C_{m_q}+C_{m_{\dot{\alpha}}}$ is typically evaluated. Specifically, C_{m_0} haracterizes the aerodynamic damping effect induced by unsteady flow generated during pitching oscillations, whereas $C_{m_{\hat{\alpha}}}$ represents the inertial damping effect associated with the acceleration of the surrounding fluid driven by vehicle oscillations. When $C_{m_{\alpha}} + C_{m_{\dot{\alpha}}}$ is negative, the overall effect provides damping, meaning that the system delivers net energy dissipation over a complete oscillation cycle, and the vehicle is considered to be dynamically stable.

3. Results

3.1. Verification of Dynamic Derivative Calculations

To verify the capability of the present code in simulating forced oscillations, reference is made to the free-oscillation wind tunnel experiments conducted at the Jet Propulsion Laboratory (JPL)[18]. The

HiSST-2025-#271 Page |4 test model is a blunt cone with a half-cone angle of 10° , a base diameter of D=133.35 mm, and a reference length defined as the total body length L=1.8838D(251.20473mm). The corresponding reference area is 0.013966124m2, and the nose bluntness ratio is R/D=0.4. The detailed geometric parameters are shown in Fig. 1, and the computational grid employed in the simulations is illustrated in Fig. 2.

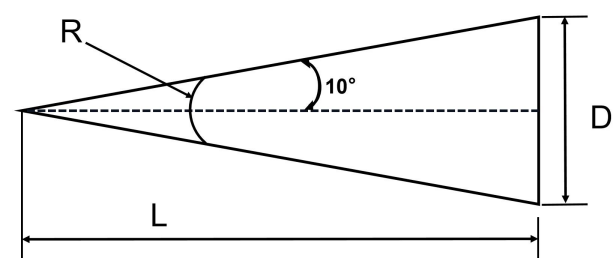


Fig 1. Geometric dimensions of the blunt-cone model

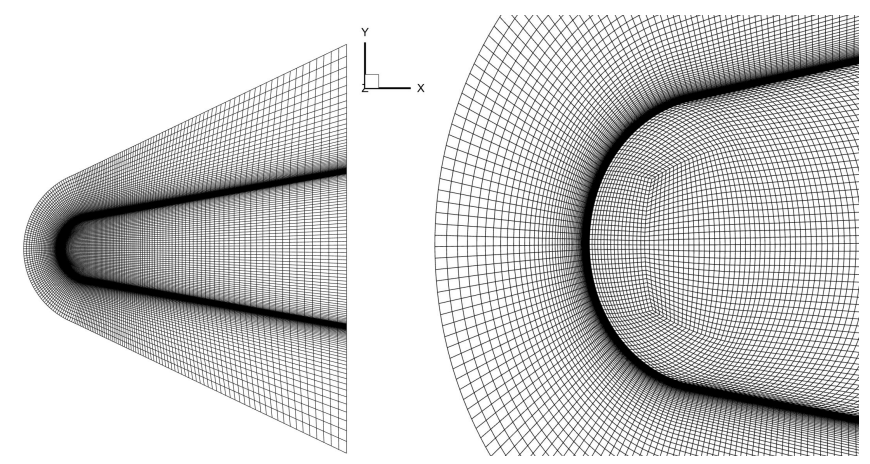


Fig 2. Computational grid for the blunt-cone model

Table 2. Computational conditions

Ма	Re	т	a ₀	Amplitude	Reduced frequency $k_{red}=\omega D/(2V^2)$	Center of gravity (x/L)
						0.604
4.0	7.5×10^6	56.7K	0°	2°	0.005	0.6336
						0.6618

Fig. 3 compares the dynamic derivatives computed by the present code at different center-of-gravity locations with the experimental data. It can be seen that the code provides a high level of accuracy in predicting dynamic derivatives.

HiSST-2025-#271 Page | 5 Effects of Boundary Layer Transition on Dynamic Stability for Hypersonic Blunt-Cone Vehicles Copyright © 2025 by author(s)

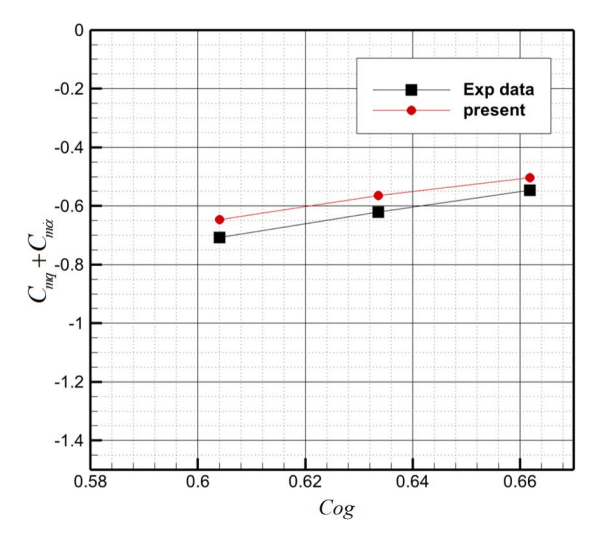


Fig 3. Comparison of dynamic derivative results

3.2. Forced pitching oscillation under hypersonic transitional flow conditions

To investigate the influence of boundary-layer transition on the dynamic stability of pitching oscillations for reentry vehicles at high altitudes, the present study is further conducted based on the flight test data of the 5° half-angle blunt cone vehicle[19] obtained in the United States.

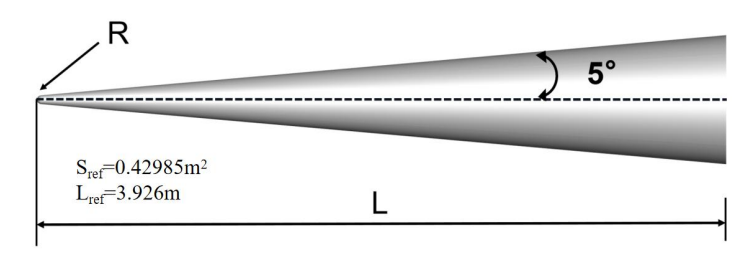


Fig 4. Geometric dimensions of the 5° half-angle blunt-cone model

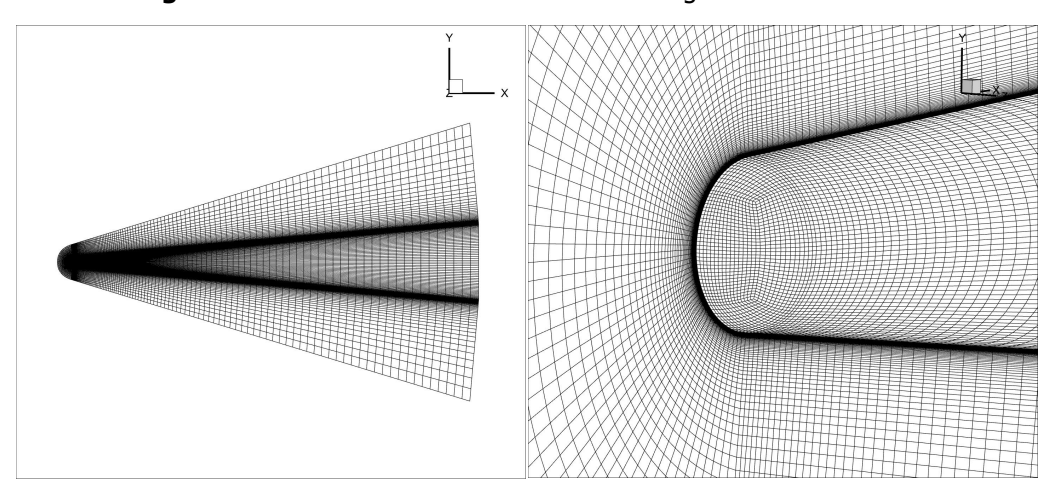


Fig 5. Computational grid for the 5° half-angle blunt-cone model

The configuration considered is a 5° half-angle blunt cone with a total length of L=396.2cm and a nose radius of R=0.254cm. The schematic of the model is shown in Fig. 4, and the computational grid is illustrated in Fig. 5. The flight experiment provided data on Reynolds number, angle of attack, and wall heat flux variation at altitudes ranging from 10 km to 50 km, as well as the heat flux distribution along the leeward meridian at different altitudes. At an altitude of 24.384 km, transition was observed to occur at x=2.1m. Fig. 6 presents the wall intermittency distribution computed using the Fu–Wang transition model. The computational conditions are summarized in Table 2. Subsequently, the heat flux along the leeward meridian was extracted and compared with the experimental measurements.

HiSST-2025-#271 Page |6 Li Jiahao. First, Wang Liang. Second, Zhao Rui. Third, Sha Xinguo. Fourth, Wang Yutang. Fifth Copyright © 2025 by author(s)

As shown in Fig. 7, the predicted transition location agrees very well with the experimental data.

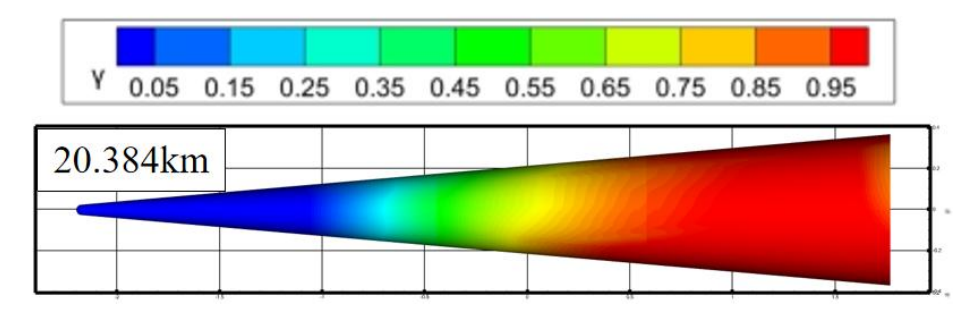


Fig 6. Distribution of wall intermittency factor

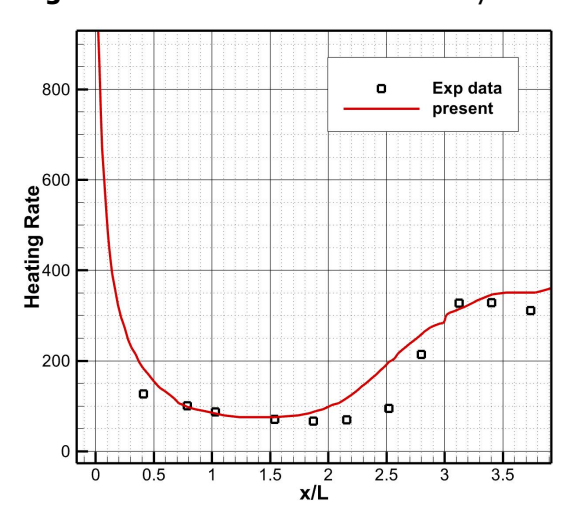


Fig 7. Leeward meridian heat flux compared with experiment

3.3. Effect of transition location on dynamic stability

From the angle-of-attack history provided by the experiment (Fig. 8), it can be observed that the most rapid variation occurs around t=458s, corresponding to a flight altitude of approximately 24km. Therefore, static transition and forced-oscillation analyses were carried out at three representative altitudes of 20km, 24km, and 28km.

Table 3. Static transition computational conditions

Altitude	Ма	Re _∞	Т	a_0	Isothermal wall
24.384km	19.2	1.755×10^7	220.96	0.5°	1000K
20km	20	3.66×10 ⁷	216.6	0.5°	1000K
24km	20	1.94×10 ⁷	220.6	0.5°	1000K
28km	20	1.033×10 ⁷	224.5	0.5°	1000K

HiSST-2025-#271 Page |7 Effects of Boundary Layer Transition on Dynamic Stability for Hypersonic Blunt-Cone Vehicles Copyright © 2025 by author(s)

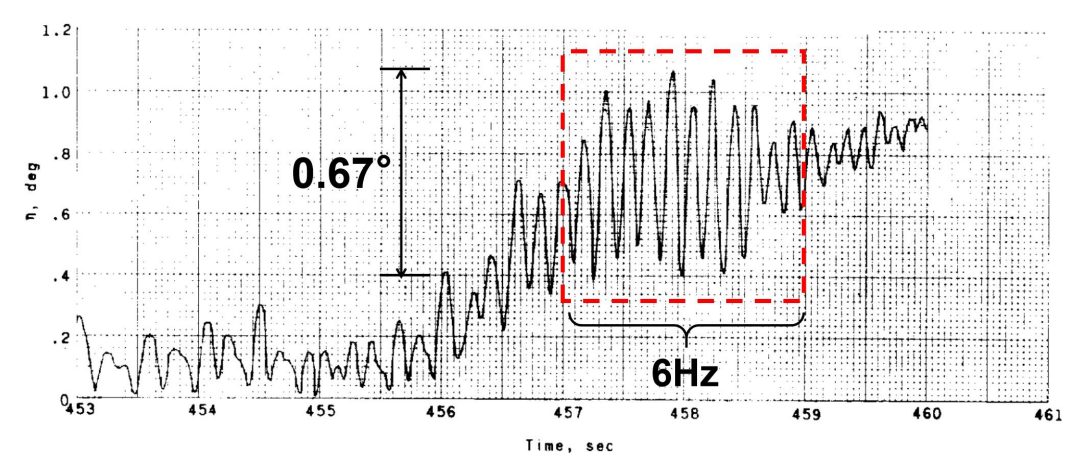


Fig 8. Time history of angle of attack

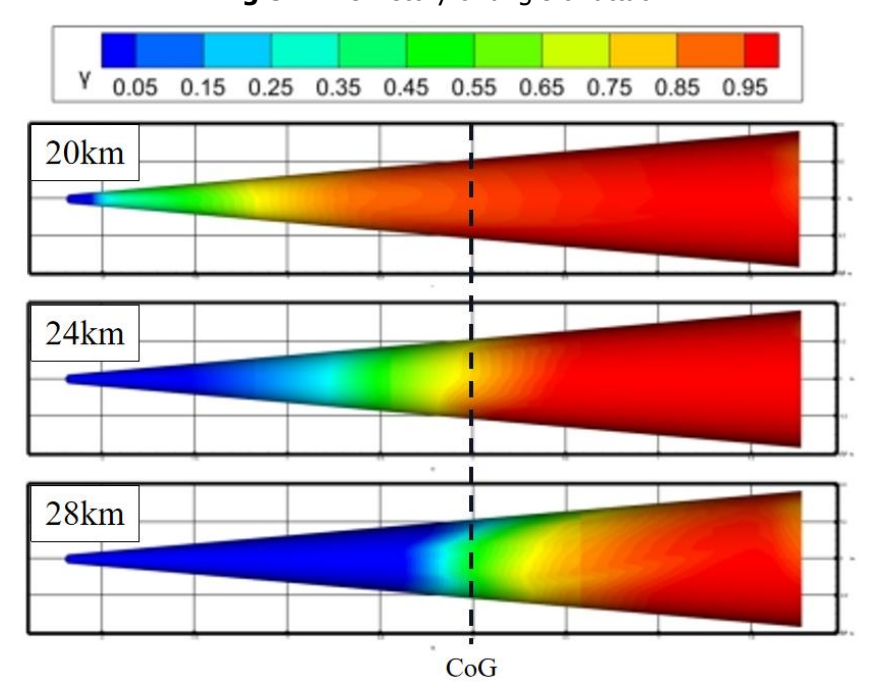


Fig 9. Distributions of wall intermittency at three different altitudes

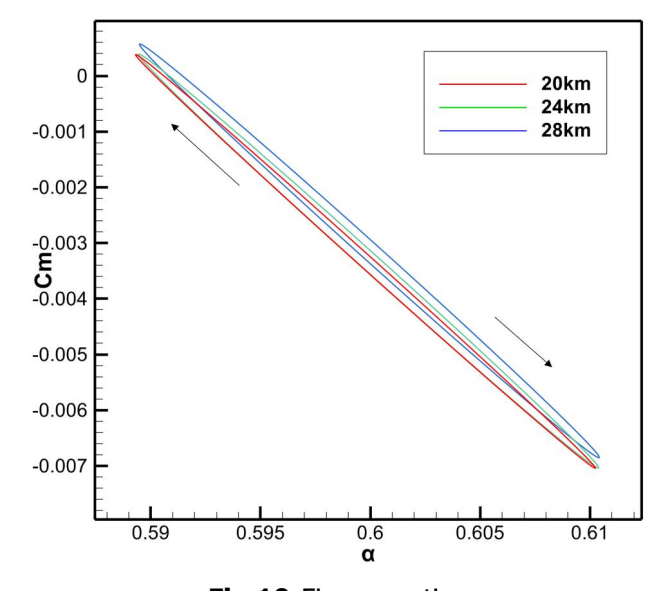


Fig 10. Figure caption

Table 4. Dvna	amic derivative	25
----------------------	-----------------	----

Altitude	C _{ma}	$C_{mq}+C_{m\dot{\alpha}}$
20km	-0.35527	1.4315
24km	-0.35489	1.7479
28km	-0.34636	1.6903

Figure 9 presents the wall intermittency distributions under static transition conditions. As the altitude changes, the external Reynolds number varies and the boundary-layer transition location shifts accordingly: at 20km the transition point lies upstream of the center of gravity(x/L=0.55), at 28km it moves downstream, and at 24km it is located nearly at the center of gravity. To examine the effect of transition location on aerodynamic stability, forced pitching-oscillation simulations were performed at these three altitudes. The reference point for pitching moment was chosen at the center of gravity , with an oscillation amplitude of 0.6° and a frequency of 6 Hz. The results show that, in all three cases, the hysteresis loops(Fig. 10) are clockwise and the dynamic derivatives(Table. 3) are positive, indicating that the vehicle is dynamically unstable under these conditions.

Among the three cases, the 24km altitude yields the largest dynamic derivative, representing the strongest dynamic instability. This can be explained by the fact that, when the transition occurs near the center of gravity, the additional aerodynamic loads generated by the turbulent boundary layer result in a highly unbalanced distribution on either side of the center of gravity. Consequently, the positive and negative contributions to the pitching moment cannot cancel each other, and the variation of aerodynamic moment with angle-of-attack perturbations is amplified, thereby intensifying dynamic instability. When the transition location moves further upstream of the center of gravity, the turbulent load acts with a shorter moment arm, and the additional aerodynamic moment exhibits partial cancellation, leading to a partial alleviation of instability. Similarly, when the transition shifts downstream of the center of gravity, the turbulent load is concentrated aft of the center, which also disturbs the balance but with a smaller resultant moment and shorter arm, producing a weaker destabilizing effect compared with the case where transition occurs exactly at the center of gravity.

These computational results are in close agreement with the experimental observations of flight attitude, which likewise revealed that the vehicle exhibited the greatest instability when the transition region was located near the center of gravity. Based on this finding, the 24km case is selected as the baseline configuration for subsequent investigations of the influence of Mach number, wall temperature condition, and oscillation amplitude on dynamic stability.

3.4. Effect of different oscillation amplitudes on dynamic stability

Figure 11 and Table 5 presents the dynamic derivatives at different oscillation amplitudes. Conventional understanding suggests that dynamic stability tends to deteriorate with increasing amplitude, since the aerodynamic response progressively departs from linear behavior. At small oscillation amplitudes, the phase lag induced by shock—boundary-layer interaction and transition migration is pronounced, leading to relatively large dynamic derivatives. However, inspection of Fig. x reveals that within the present amplitude range, the dynamic derivative exhibits an overall decreasing trend with increasing amplitude. This is attributed to the strengthening of higher-harmonic components, which reduce the contribution of the fundamental frequency component obtained through linear regression, thereby resulting in a monotonic decrease in the dynamic derivative.

It is noteworthy that a localized sharp drop in the dynamic derivative is observed around an amplitude of approximately 0.6. We hypothesize that this behavior corresponds to the crossing of a response threshold, where the phase lag between the shock wave and boundary layer, together with the coupled response of transition and laminar separation bubbles, is first significantly triggered within the oscillation cycle. This process causes a sudden increase in the equivalent viscous unsteady contribution, leading to the abrupt reduction in the linearized damping derivative. As the amplitude increases further, this "critical" behavior disappears and the curve returns to a smooth decreasing trend. The detailed mechanism underlying this phenomenon will be investigated in future work.

HiSST-2025-#271 Page |9 Effects of Boundary Layer Transition on Dynamic Stability for Hypersonic Blunt-Cone Vehicles Copyright © 2025 by author(s)

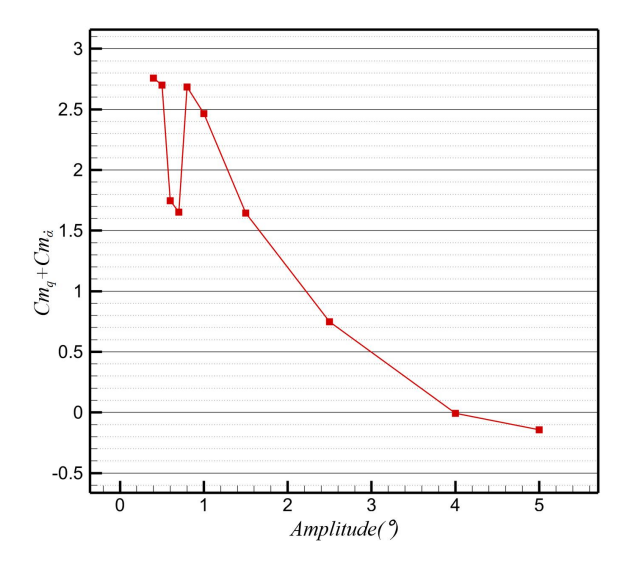


Fig 11. Amplitude-Dependent Dynamic Derivatives

Table 5. Dynamic derivatives

Amplitude	C _{ma}	C _{mq} +C _{må}
0.4	-0.34197	2.7573
0.5	-0.34449	2.6994
0.6	-0.35489	1.7478
0.7	-0.35443	1.6535
0.8	-0.34441	2.6847
1.0	-0.33923	2.4657
1.5	-0.22615	1.6438
2.5	-0.28882	0.7477
4.0	-0.24765	-0.0082
5.0	-0.23372	-0.1425

3.5. Effect of oscillation frequency on dynamic stability

Figure 12 and Table 6 presents the dynamic derivatives at different oscillation frequencies. The combined dynamic derivative $C_{m_q}+C_{m_{\dot{\alpha}}}$ exhibits a non-monotonic dependence on oscillation frequency: it decreases from low to mid frequencies and then slightly recovers at higher frequencies. Research has found that an increase in oscillation frequency enhances stability[20]. The initial decrease is governed by increasing viscous unsteadiness (shock-boundary-layer phase lag and limited transition migration), whereas the subsequent recovery is associated with the growing contribution of potential added-mass effects. This reveals a strong frequency dependence of unsteady aerodynamics rather than a simple linear trend.

HiSST-2025-#271 Page |10

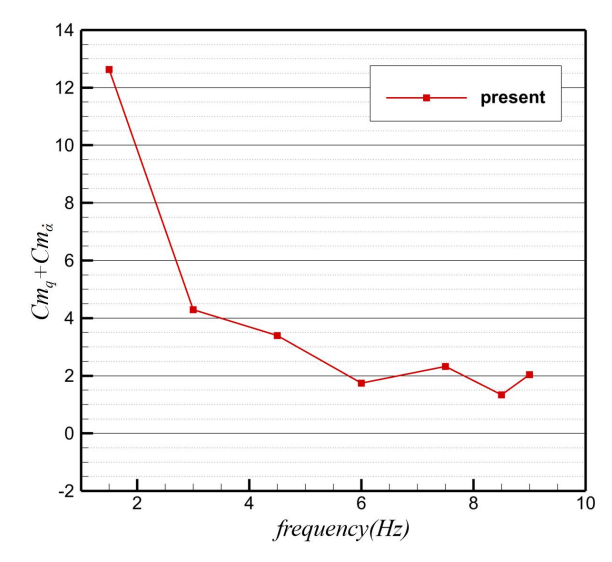


Fig 12. Frequency-dependent dynamic derivatives

Table 6. Dynamic derivatives

Frequency	C _{ma}	C _{mq} +C _{må}
1.5	-0.34480	12.6304
3.0	-0.35466	4.2919
4.5	-0.34862	3.3994
6.0	-0.35489	1.7479
7.5	-0.34529	2.3288
8.5	-0.35101	1.3394
9.0	-0.35001	2.0359

4. Conclusion

This study employed the Fu-Wang transition model and high-fidelity simulations to investigate the influence of boundary-layer transition on the dynamic stability of a hypersonic blunt-cone vehicle under forced pitching oscillations. Verification with available experimental data confirmed the reliability of the computational approach.

The main findings are as follows:

- 1) The transition location is the dominant factor for dynamic stability. The strongest instability occurs when transition coincides with the center of gravity, while upstream or downstream locations partially alleviate the destabilizing effect.
- 2) Oscillation amplitude induces an overall decrease in dynamic derivatives, with a critical sharp drop near specific amplitudes linked to shock-boundary-layer interaction and transition/separation bubble coupling.
- 3) Oscillation frequency produces a non-monotonic influence: instability increases at low frequencies due to transition migration but partially recovers at higher frequencies as added-mass effects enhance inertial damping.

Future work will extend the present analysis to three-dimensional vehicle configurations, include thermal-structural coupling, and pursue closer comparison with high-enthalpy wind tunnel data to refine transition-stability prediction and control strategies.

HiSST-2025-#271 Page |11 Effects of Boundary Layer Transition on Dynamic Stability for Hypersonic Blunt-Cone Vehicles Copyright © 2025 by author(s)

References

- 1. Knight D, Mortazavi M. Hypersonic shock wave transitional boundary layer interactions-A review[J]. Acta Astronautica, 2018, 151: 296-317.
- 2. Ceci A, Palumbo A, Larsson J, et al. Low-frequency unsteadiness in hypersonic swept shock wave-boundary layer interactions[J]. Physical Review Fluids, 2024, 9(5): 054603.
- 3. Bryan GH: Stability in aviation. Macmillan, London(1991)
- 4. Boyd TJM (2011) One hundred years of G. H. Bryan's stability in aviation. J Aeronaut Hist 4:97–115
- 5. Kessler D A, Hess A M, Obenschain K, et al. Performance of coupled physics solvers for multidisciplinary hypersonic flow simulations on several classes of computer architectures[C]//AIAA SciTech 2022 Forum. 2022: 0973.
- 6. Schuabb M, Duan L, Casper K M, et al. Hypersonic boundary-layer transition over a circular cone in a Mach 8 digital wind tunnel[J]. Journal of Fluid Mechanics, 2025, 1017: A33.
- 7. Mi B, Zhan H. Review of numerical simulations on aircraft dynamic stability derivatives[J]. Archives of Computational Methods in Engineering, 2020, 27(5): 1515-1544.
- 8. Paredes P, Venkatachari B S, Choudhari M M, et al. Toward transition modeling in a hypersonic boundary layer at flight conditions[C]//AIAA Scitech 2020 Forum. 2020: 0103.
- 9. McAlister K W. Aerodynamic Characteristics of a Large-angle Blunt Cone with and Without Fence-type Afterbodies[M]. National Aeronautics and Space Administration, 1971.
- 10. Wang L, Fu S. Modelling flow transition in a hypersonic boundary layer with Reynolds-averaged Navier-Stokes approach[J]. Science in China Series G: Physics, Mechanics and Astronomy, 2009, 52(5): 768-774.
- 11. Wang L, Zhou L. Prediction of aerodynamic characteristics of hypersonic vehicle by improved $k-\omega-\gamma$ transition model[J]. Acta Aerodynamica Sinica, 2021, 39(3): 51-61.
- 12. Yoon S, Jameson A. Lower-upper symmetric-Gauss-Seidel method for the Euler and Navier-Stokes equations[J]. AIAA journal, 1988, 26(9): 1025-1026.
- 13. Liou M S. A sequel to AUSM, Part II: AUSM+-up for all speeds[J]. Journal of computational physics, 2006, 214(1): 137-170.
- 14. Menter F R, Two-Equation Eddy-Viscosity Turbulence Models for Engineering Applications, AIAA Journal, Vol. 32, No. 8, August 1994, pp. 1598-1605
- 15. Zhou L, Yan C, Hao Z H. Improved $k-\omega-\gamma$ model for hypersonic boundary layer transition prediction[J]. International Journal of Heat and Mass Transfer, 2016, 94: 380-389.
- 16. Etkin B, Reid LD (1996) Dynamics of flight: stability and control. Wiley, New York, p 107
- 17. Etkin B (2012) Dynamics of atmospheric flight. Dover Publications, New York, p 125
- 18. Prislin R H. High amplitude dynamic stability characteristics of blunt 10-degree cones[J]. AIAA Paper, 1966, 465.
- 19. Wright R L, Zoby E V. Flight Measurements of Boundary-Layer Transition on A 5 Degree Half-Angle Cone at A Free-Stream Mach Number of 20 (Reentry F)[R]. No. Report Number: L-7506. 1971.
- 20. Shengxi T , Yanming F , Feng G ,et al.Evaluation of Dynamic Stability Derivatives for Hypersonic Vehicle[J].IOP Conference Series Materials Science and Engineering, 2020, 887:012037.DOI:10.1088/1757-899X/887/1/012037.

HiSST-2025-#271

Page | 12